ADVANCED FUNCTIONAL MATERIALS
www.afm-journal.de

A New Strategy to Build a High-Performance P′2-Type Cathode Material through Titanium Doping for Sodium-Ion Batteries

Yun Ji Park, Ji Ung Choi, Jae Hyeon Jo, Chang-Heum Jo, Jongsoon Kim, and Seung-Taek Myung**

Herein, Ti^{4+} in P′2-$Na_{0.67}[(Mn_{0.78}Fe_{0.22})_{0.9}Ti_{0.1}]O_2$ is proposed as a new strategy for optimization of Mn-based cathode materials for sodium-ion batteries, which enables a single phase reaction during de-/sodiation. The approach is to utilize the stronger Ti–O bond in the transition metal layers that can suppress the movements of Mn–O and Fe–O by sharing the oxygen with Ti by the sequence of Mn–O–Ti–O–Fe. It delivers a discharge capacity of ≈180 mAh g^{-1} over 200 cycles (86% retention), with S-shaped smooth charge–discharge curves associated with a small volume change during cycling. The single phase reaction with a small volume change is further confirmed by *operando* synchrotron X-ray diffraction. The low activation barrier energy of ≈541 meV for Na^+ diffusion is predicted using first-principles calculations. As a result, $Na_{0.67}[(Mn_{0.78}Fe_{0.22})_{0.9}Ti_{0.1}]O_2$ can deliver a high reversible capacity of ≈153 mAh g^{-1} even at 5C (1.3 A g^{-1}), which corresponds to ≈85% of the capacity at 0.1C (26 mA g^{-1}). The nature of the sodium storage mechanism governing the ultrahigh electrode performance in a full cell with a hard carbon anode is elucidated, revealing the excellent cyclability and good retention (≈80%) for 500 cycles (111 mAh g^{-1}) at 5C (1.3 A g^{-1}).

1. Introduction

Lithium-ion batteries (LIBs) have attracted significant attention over the past decades because of their relatively high energy density and fast charge–discharge capability. Since the 2000s, research in this field has become increasingly active because of the rapid spread of portable devices.[1] However, concerns over the depletion of lithium metals and the drastic increase in the demands for LIBs causing a surge in lithium prices are becoming important issues.[1,2] As a promising alternative to LIBs, sodium-ion batteries (SIBs) are being revisited because of the abundance of sodium resources and the similar chemistries of SIBs and LIBs, which both adopt insertion/extraction reactions.[3–5] Although SIBs have intrinsic drawbacks, such as their low operation voltages relative to those of LIBs and the difficulty of ready insertion of sodium ions because of the larger size of Na^+ ions (1.02 Å) compared with Li^+ ions (0.76 Å), these difficulties can be mitigated with a high capacity to compensate for the low operation voltage.[5]

Layered cathode material for SIBs (Na_xMeO_2) has received particular attention owing to their relatively high capacity and structural stability. Layered Na_xMeO_2 (x = 0.5–1 and Me; transition metal) consist of MeO_2 layers sharing edges with MeO_6 octahedra were classified into two groups based on structure: trigonal prismatic (P type: P2, P3, and P′2) and octahedral (O type: O3).[6] The differences in these structures are attributed to sodium ions being respectively located at the district trigonal prismatic or octahedral crystallographic sites sandwiched between the MeO_2 sheets. Among them, many works have introduced Mn-based cathode materials, mainly P2-type materials, in which sodium ions are located at prismatic sites with an AABB oxygen stacking sequence, because of their low cost, good performance, and nontoxicity.[7,8] Recently, many works about P2-type materials have been investigated such as Na_xMnO_2,[7,9] Na_xCoO_2,[10] Na_xVO_2,[11] $Na_x[Ni,Mn]O_2$,[12] $Na_x[Fe,Mn]O_2$,[13] $Na_x[Ni,Fe,Mn]O_2$,[14] $Na_x[Mg,Mn]O_2$,[15] $Na_x[Ni,Mg,Mn]O_2$.[16] P2-type materials crystallize in a hexagonal structure; however, the transition metal layers can be distorted at higher temperature with stabilization in an orthorhombic structure (represented as P′2) albeit with the same chemical composition.[17,18] Many works have introduced Mn-based cathode materials, mainly P2-type materials, in which sodium ions are located at prismatic sites with an AABB oxygen stacking sequence, because of their low cost, good performance, and nontoxicity.[7,8] P2-type materials crystallize in a hexagonal structure; however, the transition metal layers can be distorted at higher temperature with stabilization in an orthorhombic structure (represented as P′2) albeit with the same chemical composition.[17,18] The elongation of the *b*-axis in the P2 layer structure distorts the structure toward the P′2 phase, where the *b*-axis parameter in the P′2 structure is longer

Y. J. Park, J. U. Choi, J. H. Jo, C.-H. Jo, Prof. J. Kim, Prof. S.-T. Myung
Department of Nano Technology and Advanced Materials Engineering & Sejong Battery Institute
Sejong University
Seoul 05006, South Korea
E-mail: jongsoonkim@sejong.ac.kr; smyung@sejong.ac.kr
The ORCID identification number(s) for the author(s) of this article can be found under https://doi.org/10.1002/adfm.201901912.

DOI: 10.1002/adfm.201901912

than $b = \sqrt{3}a$ in the P2 structure. $Na_{2/3}MnO_2$ is a well-known P′2-type orthorhombic structure, as reported by Stoyanova et al.[7] Despite the presence of Jahn–Teller distortion in P′2-type orthorhombic $Na_{2/3}MnO_2$, the resulting electrochemical cyclability is better than that of P2-type hexagonal $Na_{2/3}MnO_2$, as demonstrated by Kumakura et al.[18,19] The reason for this improvement remains unknown; however, higher crystallinity is speculated to be a possible reason because the P′2 structure usually forms above 1000 °C. In addition, continuous phase transitions are considered a possible reason for the capacity fading upon cycling. Kumakura et al.[18,19] and Choi et al.[17,20] reported the suppression of these phase transitions upon doping with a small amount of divalent elements such as Cu^{2+} and Ni^{2+}, resulting in exceptionally high capacity retention; specifically, 86% capacity retention after doping with Cu^{2+} and 94% capacity retention after doping with Ni^{2+} in $Na_{2/3}[M_xMn_{1-x}]O_2$ (M: Cu and Mn). Despite the excellent cycling stability of these electrodes, their rate performances require further improvement. Indeed, the main drawback of this material is the large volume change accompanying the P′2–OP4 phase transition, which hinders facile insertion of sodium ions into the structure at high rates. Recently, we investigated Fe substitution in the P′2 structure, namely, in P′2-$Na_{0.67}[Fe_{0.2}Mn_{0.8}]O_2$ compounds.[17,20] The introduction of Fe resulted in improvement of the electrode performance owing to suppression of the P′2–OP4 phase transition.[20] Furthermore, it is anticipated that the resulting capacity retention and rate capability can be further improved if the structure can be maintained in the P′2 phase in the operation voltage window. The introduction of an additional substituent is needed to further minimize the phase transition of P′2-$Na_{0.67}[Fe_xMn_{1-x}]O_2$ during cycling. In this study, titanium doping was selected as a new strategy for the optimization of Mn-based cathode material with high rate capability. Even though tetravalent Ti is electrochemically inactive since the *d* orbital is empty, the tetravalent Ti as a form of TiO_2 shows a low Gibbs free energy for formation at 298K ($\Delta_f G_{298K} = -888$ kJ mol^{-1}),[21] which is much lower than that of $Mn^{4+}O_2$ ($\Delta_f G_{298K} = -465.2$ kJ mol^{-1}).[21] From the anticipation, we introduce Ti^{4+} in P′2-$Na_{0.67}[(Mn_{0.78}Fe_{0.22})_{0.9}Ti_{0.1}]O_2$ as a new strategy for optimization of Mn-based cathode materials for SIBs. The stronger Ti–O bonds may suppress the movements of Mn–O and Fe–O by sharing the oxygen with Ti, presumably followed by the sequence of Mn–O–Ti–O–Fe in the transition metal layers. Ti-doped P′2-$Na_{0.67}[(Mn_{0.78}Fe_{0.22})_{0.9}Ti_{0.1}]O_2$ is successfully synthesized via spray pyrolysis, and a homogeneous active material with improved cycling performance is obtained. Unexpectedly, the Ti-substituted electrode delivers a high discharge capacity (≈153 mAh g^{-1}) at a rate of 5C (1300 mA g^{-1}). In addition, the introduction of Ti^{4+} in the P′2-$Na_{0.67}[(Mn_{0.78}Fe_{0.22})_{0.9}Ti_{0.1}]O_2$ successfully suppresses the phase transition from P′2 to OP4, as evidenced by *operando* synchrotron X-ray diffraction (SXRD), which revealed the occurrence of a single phase reaction during cycling. The suppression of the P′2 to OP4 phase transition may have contributed to the delivery of high capacity even at high rates and excellent capacity retention with prolonged cycling. The effect of Ti^{4+} on the electrode performance and occurrence of the single phase reaction were unveiled using bond valence sum (BVS) energy mapping and first-principles calculations. Finally, $Na_{0.67}[(Mn_{0.78}Fe_{0.22})_{0.9}Ti_{0.1}]O_2$ // hard carbon full cells show excellent capacity retention of ≈80% for 500 cycles (111 mAh g^{-1}) at 5C (1.3 A g^{-1}). Various types of anode materials, including nanostructured materials, carbon-based materials, metals, and oxide/sulfide, have been investigated for SIBs.[4,22] Also, carbon-based materials, including graphite, hard carbon, are inexpensive and widely applicable.[23] Among them, hard carbon with a large interlayer *d*-spacing is favorable for the storage of large sodium ions and exhibits a reasonable capacity approximately 200 mAh g^{-1}.[24] For the reason, hard carbon materials has chosen as the counterpart of the $Na_{0.67}[(Mn_{0.78}Fe_{0.22})_{0.9}Ti_{0.1}]O_2$ cathode for long term cycle test in this study.

2. Results and Discussion

The crystal structure of as-synthesized P′2-$Na_{0.67}[(Mn_{0.78}Fe_{0.22})_{0.9}Ti_{0.1}]O_2$ was analyzed using Rietveld refinement of XRD data (**Figure 1**a; Table S1, Supporting Information). The Bragg peak positions and intensities were consistent with the orthorhombic P′2 layered structure with *Cmcm* space group.[17–20] As observed in Table S1 (Supporting Information), no impurities were detected, indicating that Fe^{3+} and Ti^{4+} ions were introduced into the transition metal sites. The resulting crystal structure based on the refined data is drawn in the inset of Figure 1a. A bright-field transmission electron microscopy (TEM) image and the corresponding energy-dispersive X-ray spectroscopy (EDS) mapping data for P′2-$Na_{0.67}[(Mn_{0.78}Fe_{0.22})_{0.9}Ti_{0.1}]O_2$ powder are presented in Figure 1b. The EDS mapping results indicate that Na, Mn, Fe, and Ti elements were uniformly distributed.

Compared with Ti-free P′2-$Na_{0.67}[(Mn_{0.78}Fe_{0.22})_{1-x}Ti_x]O_2$,[20] a slight increase in the lattice parameters was observed for $Na_{0.67}[(Mn_{0.78}Fe_{0.22})_{0.9}Ti_{0.1}]O_2$ (Table S1, Supporting Information). The lattice parameter increase is most likely related to the difference in the ionic radii of Mn^{3+} (0.645 Å), Mn^{4+} (0.54 Å), and Ti^{4+} (0.604 Å).[25] Namely, Ti^{4+} prefers to replace Mn^{4+} rather than Mn^{3+} and Fe^{3+} (0.645 Å), presumably to preserve the charge balance of the compound. For the replacement of Mn^{4+} by Ti^{4+}, the increase in the lattice parameters is understood to result from the larger ionic radius of Ti^{4+} than Mn^{4+}. The Ti K-edge spectra (Figure 1c) clearly reveal that the average oxidation state of Ti is identical to that of the $Ti^{4+}O_2$ reference, indicating that Ti appears as Ti^{4+}. In addition, the Fe K-edge spectrum indicates that the average oxidation state of Fe is Fe^{3+} in the compound (Figure 1d). A slight shift toward lower photon energy in the Mn K-edge spectra with Ti substitution (Figure 1e), suggesting a decrease in the average oxidation state of Mn. This decrease can be interpreted as the substitution of Ti^{4+} for Mn^{4+} such that the total amount of Mn^{4+} was reduced while the concentration of Mn^{3+} remained constant. In summary, it is apparent that the replacement of Mn^{4+} by Ti^{4+} resulted in an increase in the lattice parameters and slight decrease in the oxidation state of Mn in $Na_{0.67}[(Mn_{0.78}Fe_{0.22})_{0.9}Ti_{0.1}]O_2$ compared with those in $Na_{0.67}MnO_2$ and Ti-free $Na_{0.67}[(Mn_{0.78}Fe_{0.22})_{1-x}Ti_x]O_2$ ($x = 0$).[17,20]

To verify the theoretical properties of $Na_x[(Mn_{0.78}Fe_{0.22})_{0.9}Ti_{0.1}]O_2$ as a cathode material for SIBs, we performed first-principles calculations based on the structural information

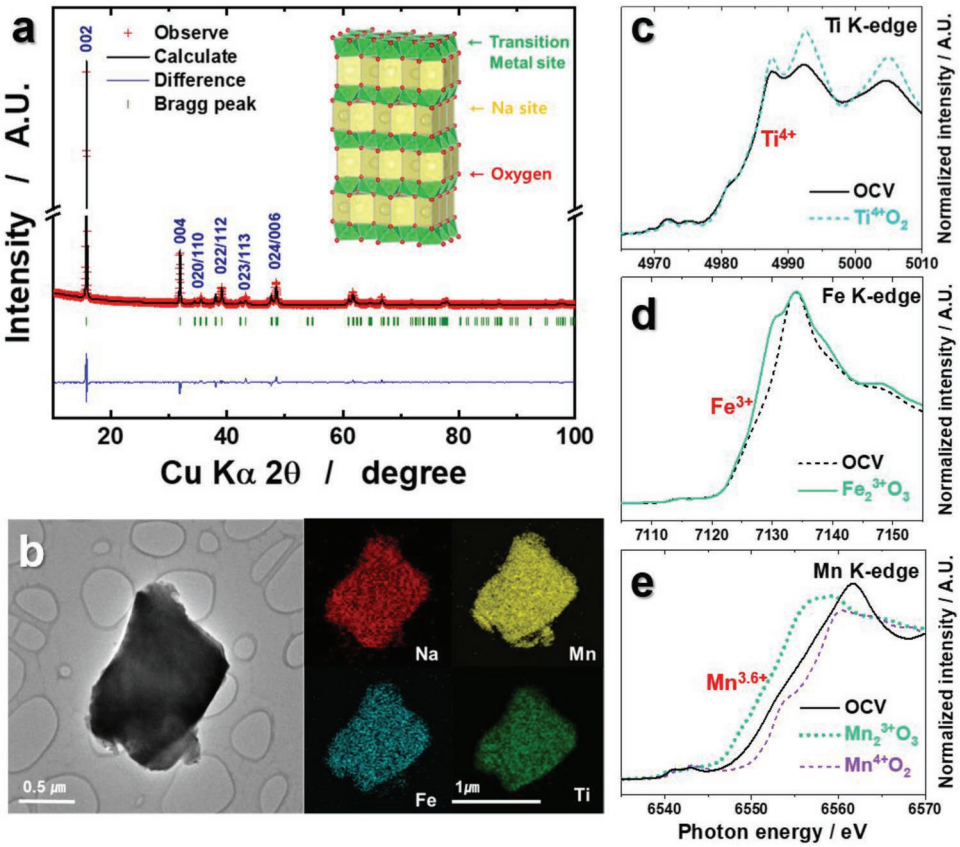

Figure 1. a) Rietveld refinement results for powder XRD patterns (inset: schematic illustrations based on the refined data). b) TEM image and EDS mapping image. XANES spectra for c) Ti K-edge, d) Fe K-edge, and e) Mn K-edge of P′2-$Na_{0.67}[(Mn_{0.78}Fe_{0.22})_{0.9}Ti_{0.1}]O_2$ powder.

obtained using Rietveld refinement of the XRD data. **Figure 2**a presents the convex hull plot of the formation energies of $Na_x[(Mn_{0.78}Fe_{0.22})_{0.9}Ti_{0.1}]O_2$ ($0 \le x \le 1$) for various Na^+/vacancy configurations with various stable intermediate phases. The results indicate the occurrence of a single-phase reaction of $Na_x[(Mn_{0.78}Fe_{0.22})_{0.9}Ti_{0.1}]O_2$ during the charging/discharging process. The predicted redox potentials for each composition of $Na_x[(Mn_{0.78}Fe_{0.22})_{0.9}Ti_{0.1}]O_2$ were determined using the following equation

$$V = \frac{E[Na_{x2}[(Mn0.78Fe0.22)0.9Ti0.1]O_2] - E[Na_{x1}[(Mn0.78Fe0.22)0.9Ti0.1]O_2] - (x_2 - x_1)E[Na]}{(x_2 - x_1)F} \quad (1)$$

where V is the average voltage between x_2 and x_1; $E[Na_x[(Mn_{0.78}Fe_{0.22})_{0.9}Ti_{0.1}]O_2]$ and E(Na) are the formation energies for the most stable configuration of $Na_x[(Mn_{0.78}Fe_{0.22})_{0.9}Ti_{0.1}]O_2$ and Na metal, respectively; and F is the Faraday constant. The Na content in $Na_x[(Mn_{0.78}Fe_{0.22})_{0.9}Ti_{0.1}]O_2$ was predicted to be less than 0.125 mol. Further Na deintercalation from the structure would require much higher redox potential than the other Na deintercalation processes, and the additional Na intercalation into the $Na_{0.875}[(Mn_{0.78}Fe_{0.22})_{0.9}Ti_{0.1}]O_2$ structure occurred at much lower redox potential than the other Na intercalation processes, which implies that ≈0.7 mol Na ions might be reversibly de/intercalated from/into the $Na_x[(Mn_{0.78}Fe_{0.22})_{0.9}Ti_{0.1}]O_2$ structure. In Figure 2b, the predicted redox potentials of $Na_x[(Mn_{0.78}Fe_{0.22})_{0.9}Ti_{0.1}]O_2$ and the galvanostatic intermittent titration technique (GITT) charge/discharge curves in the voltage range between 1.5 and 4.3 V (vs Na^+/Na) are compared. The predicted redox potentials of $Na_x[(Mn_{0.78}Fe_{0.22})_{0.9}Ti_{0.1}]O_2$ ($0.125 \le x \le 0.875$) were consistent with the experimentally measured voltage profiles. A total of ≈0.875 mol Na ions, corresponding to a specific capacity of ≈180 mAh g^{-1}, may be accommodated by $Na_x[(Mn_{0.78}Fe_{0.22})_{0.9}Ti_{0.1}]O_2$ during the charging/discharging process.

From the first-principles calculation data, we obtained further information on the structural change of $Na_x[(Mn_{0.78}Fe_{0.22})_{0.9}Ti_{0.1}]O_2$ during the Na^+ de/intercalation process. Figure 2c shows the predicted crystal structures for $Na_x[(Mn_{0.78}Fe_{0.22})_{0.9}Ti_{0.1}]O_2$ ($x = 0.125$, 0.25, 0.5, 0.75, and 0.875) with each c-axis parameter. Upon Na^+ deintercalation from the structure, the c-axis parameters of $Na_x[(Mn_{0.78}Fe_{0.22})_{0.9}Ti_{0.1}]O_2$ gradually increased from ≈11.02 to ≈11.53 Å owing to the repulsive force of the two adjacent oxygen layers along the c-axis

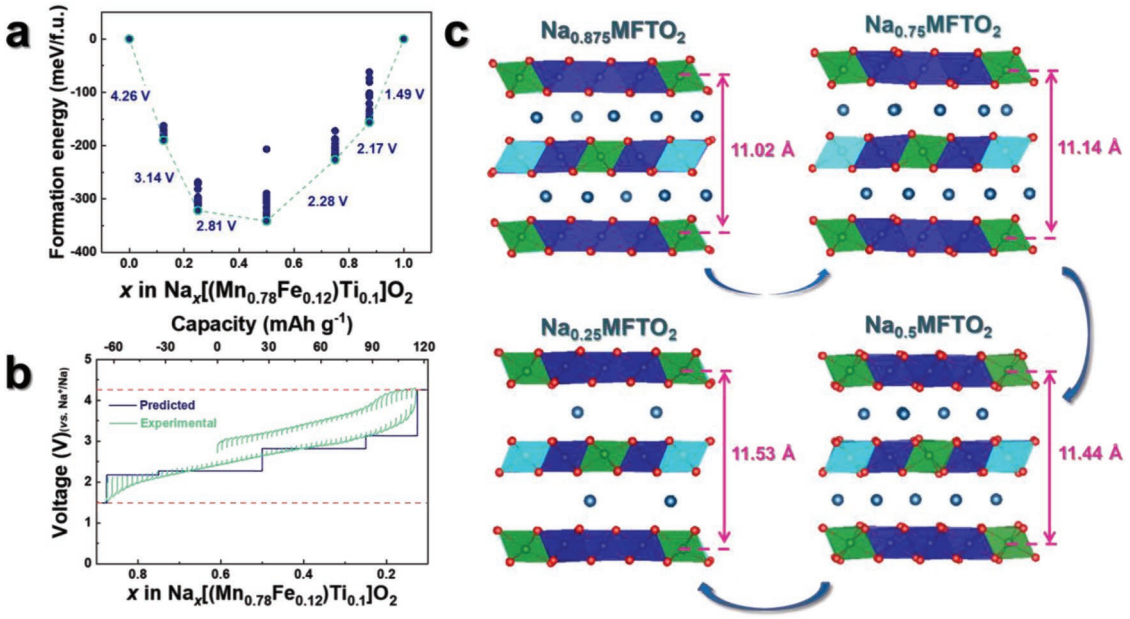

Figure 2. a) Convex-hull plot of the formation energies of $Na_x[(Mn_{0.78}Fe_{0.22})_{0.9}Ti_{0.1}]O_2$ ($0 \le x \le 1$) with the predicted redox potentials. b) Comparison of the predicted redox potential and experimentally measured GITT profile for $Na_x[(Mn_{0.78}Fe_{0.22})_{0.9}Ti_{0.1}]O_2$. c) Structural change of $Na_x[(Mn_{0.78}Fe_{0.22})_{0.9}Ti_{0.1}]O_2$ predicted through first-principles calculations.

(O^{2-}–O^{2-} repulsion) commonly observed in various layered-type electrode materials for LIBs and SIBs.[26] Interestingly, it was predicted that although a large amount of Na ions (≈0.75 mol) are de/intercalated from/into the structure, the difference in the *c*-axis parameters between $Na_{0.125}[(Mn_{0.78}Fe_{0.22})_{0.9}Ti_{0.1}]O_2$ and $Na_{0.875}[(Mn_{0.78}Fe_{0.22})_{0.9}Ti_{0.1}]O_2$ was limited to ≈4.6%, which is relatively small compared with the structural change observed for other layered-type cathode materials for SIBs. We speculate

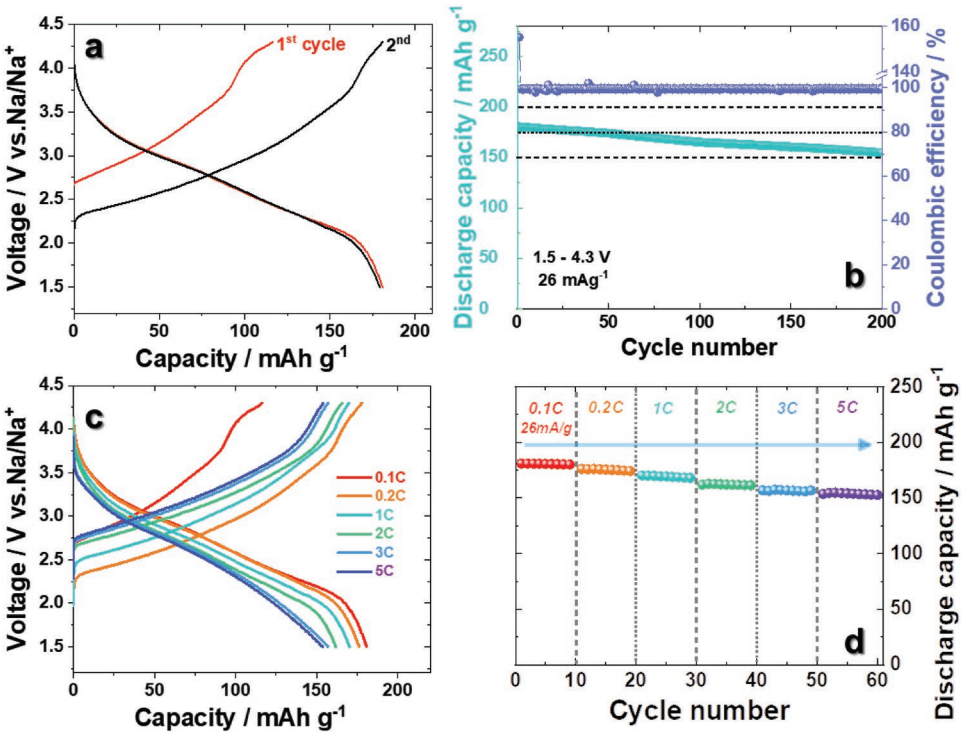

Figure 3. a) Charge–discharge voltage profiles, b) cycling performance during 200 cycles, c) capacity versus voltage curves measured at 0.1, 0.2, 1, 2, 3, and 5C, and d) corresponding cyclability of P′2-$Na_{0.67}[(Mn_{0.78}Fe_{0.22})_{0.9}Ti_{0.1}]O_2$ electrodes.

that the small structural change in $Na_x[(Mn_{0.78}Fe_{0.22})_{0.9}Ti_{0.1}]O_2$ during the charging/discharging process is associated with the weakened Jahn–Teller distortion by Mn^{3+}. As shown in Figure S1 (Supporting Information), the Mn–O bonding distances for $Na_{0.75}[(Mn_{0.78}Fe_{0.22})_{0.9}Ti_{0.1}]O_2$ and $Na_{0.75}MnO_2$. MnO_6 octahedra in the $Na_{0.75}[(Mn_{0.78}Fe_{0.22})_{0.9}Ti_{0.1}]O_2$ structure were predicted to be less distorted than those in the $Na_{0.75}MnO_2$ structure, which implies that substitution of Mn ions with Fe^{3+} and Ti^{4+} ions mitigates the effect of Jahn–Teller distortion by Mn^{3+} in the oxide lattice. Furthermore, the structural stability of Na_xMnO_2 has been reported to be greatly affected by Jahn–Teller distortion by Mn^{3+}, which may result in a particular Na/vacancy configuration of Na_xMnO_2 depending on the Na content in the structure and produce a step-wise voltage profile of Na_xMnO_2 during the Na de/intercalation process.[18] The agreement between the calculated and experimental charge/discharge curves for $Na_x[(Mn_{0.78}Fe_{0.22})_{0.9}Ti_{0.1}]O_2$ indicates that the smoother and more sloppy shape compared with the voltage profiles of Na_xMnO_2 can be attributed to the single phase reaction and dilution of the Jahn–Teller effects in the structure (Figure S1, Supporting Information).[17,20]

The electrochemical performance of $Na_{0.67}[(Mn_{0.78}Fe_{0.22})_{0.9}Ti_{0.1}]O_2$ was evaluated at 0.1C (26 mA g^{-1}) in the range of 1.5–4.3 V. The first charge and discharge capacities of $Na_{0.67}[(Mn_{0.78}Fe_{0.22})_{0.9}Ti_{0.1}]O_2$ were 116 and 180 mAh g^{-1}, respectively, which are lower than those for $Na_{2/3}MnO_2$,[17,20] because Mn and Fe ions, but not the substituted Ti ions, participate in the electrochemical reaction in the range of 1.5–4.3 V (**Figure 3**a). Whereas several voltage plateaus are observed for $Na_{2/3}MnO_2$ owing to the P′2–OP4 phase transition,[17,18] simple sloppy curves were observed for the present $Na_{0.67}[(Mn_{0.78}Fe_{0.22})_{0.9}Ti_{0.1}]O_2$. In addition, the small broad hill at 3.5 V for $Na_{2/3}MnO_2$[17,20] is an indicator of the P′2 to OP4 phase transition[17,18]; however, this feature was not observed for the present $Na_{0.67}[(Mn_{0.78}Fe_{0.22})_{0.9}Ti_{0.1}]O_2$ during charging, which implies that the introduction of Ti suppresses this structural change. This structural stability contributes to the excellent reversible capacity with a capacity retention of 86% over 200 cycles (Figure 3b). The rate capability was evaluated at rates ranging from 0.1C (26 mA g^{-1}) to 5C (Figure 3c–d). The discharge capacity of $Na_{0.67}[(Mn_{0.78}Fe_{0.22})_{0.9}Ti_{0.1}]O_2$ was 180, 176, 170, 161, 156, and 153 mAh g^{-1} at 0.1, 0.2, 1, 2, 3, and 5C, respectively. The high capacity achieved at 5C (≈85% of that delivered at 0.1C) is especially noteworthy and is the highest among P2 and P′2 layered compounds reported in the literature.[8,17–20,27]

To better understand the superior cyclability and rate capability of $Na_{0.67}[(Mn_{0.78}Fe_{0.22})_{0.9}Ti_{0.1}]O_2$, we verified the activation barrier energy for Na^+ diffusion in this structure using the nudged elastic band (NEB) method based on first-principles calculations. As shown in **Figure 4**, an activation barrier energy of ≈541 meV was predicted to be required for Na^+ diffusion along the $Na1_1$–$Na1_2$ pathway in the *ab* plane, which indicates that facile Na^+ diffusion occurs into/out of the $Na_{0.67}[(Mn_{0.78}Fe_{0.22})_{0.9}Ti_{0.1}]O_2$ structure.

To confirm the effects of Fe and Ti substitution on the structure during cycling, *operando* SXRD measurements of $Na_{0.67}[(Mn_{0.78}Fe_{0.22})_{0.9}Ti_{0.1}]O_2$ were performed, as shown in **Figure 5**a. The electrochemical cell was charged/discharged at 0.1C (26 mA g^{-1}) in the voltage range of 1.5–4.3 V. The phase transition from the P′2 to OP4 structure generally occurs for P′2 compounds on charge.[17–20] In contrast, for the present $Na_{0.67}[(Mn_{0.78}Fe_{0.18})Ti_{0.1}]O_2$, the P′2 phase structure was maintained after charging to 4.3 V. More specifically, the P′2 (002) peak shifted to lower angle and the (110) and (112) peaks shifted to higher angle during charging without the occurrence of a phase transition. On discharge, the (002) peak shifted back to higher angle, and the (110) and (112) peaks shifted back to lower angles. The variation in the *c*-axis parameter was caused by O^{2-}–O^{2-} repulsion in the interlayers resulting from the insertion/extraction of sodium ions, and the changes in the *a*- and *b*-axis parameters resulted from the variation in the oxidation state of the transition metal and mainly affected the shift of the (110) peak. The reversible phenomena were observed on discharge (Figure 5b). It is notable that the volume change was only 1.45% between the fresh state and the electrode charged to 4.3 V; this is the first time such a minimal variation in volume has been reported for O3-,[28,29] P2-,[12,18,27] or P′2-type[17–20] layered cathode materials, to the best of our knowledge. The *operando* SXRD data confirmed that the original P′2 phase was maintained during charge and discharge. As shown

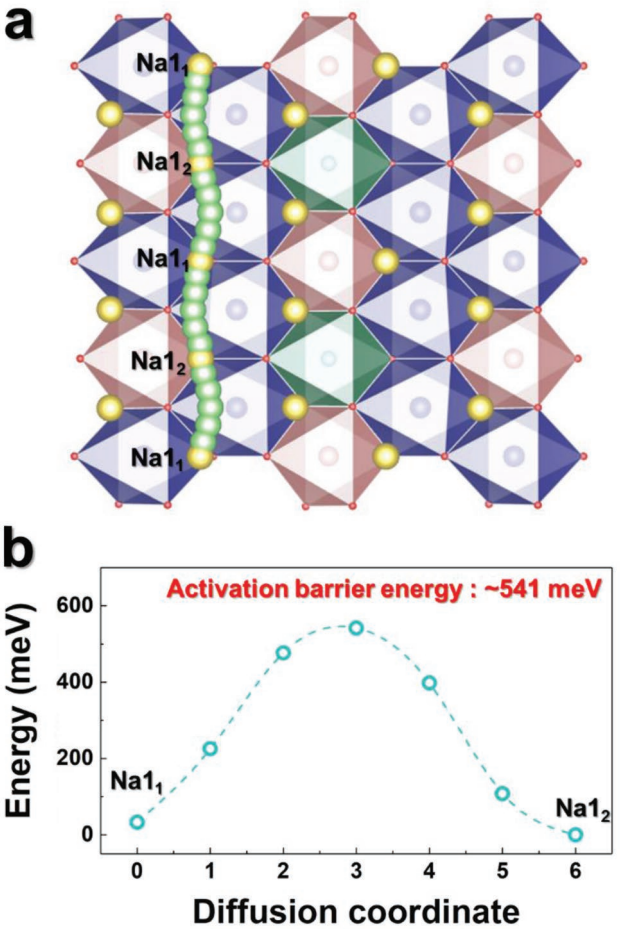

Figure 4. a) Predicted $Na1_1$–$Na1_2$ diffusion pathway in $Na_{0.67}[(Mn_{0.78}Fe_{0.22})_{0.9}Ti_{0.1}]O_2$ structure. b) Activation barrier energy for Na^+ diffusion in $Na_{0.67}[(Mn_{0.78}Fe_{0.22})_{0.9}Ti_{0.1}]O_2$ predicted using NEB method based on first-principles calculations.

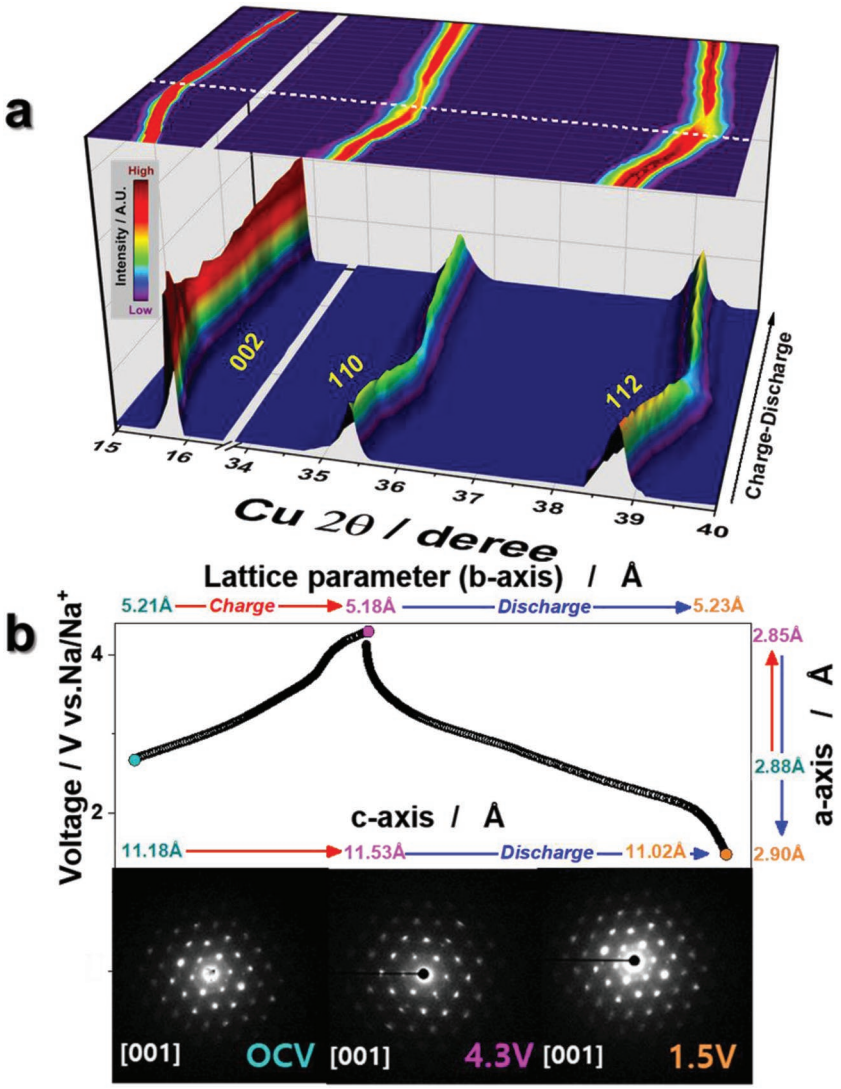

Figure 5. a) *Operando* XRD patterns of P′2-$Na_{0.67}[(Mn_{0.78}Fe_{0.22})_{0.9}Ti_{0.1}]O_2$ electrodes in Na cell (2θ value was transformed to $\lambda = 1.5418$ Å). b) Variation in lattice parameters calculated from *operando* XRD patterns (top) and SAED patterns (bottom) of P′2-$Na_{0.67}[(Mn_{0.78}Fe_{0.22})_{0.9}Ti_{0.1}]O_2$ electrodes: OCV, fully charged to 4.3 V, and fully discharged to 1.5 V.

in Figure S2 (Supporting Information), the ex situ XRD clearly verified that the present P′2-$Na_{0.67}[(Mn_{0.78}Fe_{0.22})_{0.9}Ti_{0.1}]O_2$ maintained the original structure, although some broadening of the peaks were observed when charged to 4.3 V. Selected-area electron diffraction (SAED) patterns were obtained to further evaluate the structural evolution of the $Na_{0.67}[(Mn_{0.78}Fe_{0.22})_{0.9}Ti_{0.1}]O_2$ electrode for the fresh, fully charged (4.3 V), and fully discharged (1.5 V) states. Figure 5b presents SAED patterns of the $Na_{0.67}[(Mn_{0.78}Fe_{0.22})_{0.9}Ti_{0.1}]O_2$ electrode in the direction normal to the layer planes. The SAED pattern indexed to the [001] zone of the P′2 structure agrees well with the XRD data.

To confirm the change in the oxidation states of Mn, Fe, and Ti in $Na_{0.67}[(Mn_{0.78}Fe_{0.22})_{0.9}Ti_{0.1}]O_2$ in the first cycle, X-ray absorption near-edge structure (XANES) spectra were obtained for the fresh, fully charged (4.3 V), and fully discharged (1.5 V) electrodes. **Figure 6**a presents the Mn K-edge spectra of $Na_{0.67}[(Mn_{0.78}Fe_{0.22})_{0.9}Ti_{0.1}]O_2$; Mn_2O_3 (Mn^{3+}) and MnO_2 (Mn^{4+}) spectra were used as reference spectra to analyze the change in the Mn oxidation states. The K-edge spectra of Mn moved between 3+ and 4+ throughout the redox reaction, indicating that Mn participates in the electrochemical reaction in $Na_{0.67}[(Mn_{0.78}Fe_{0.22})_{0.9}Ti_{0.1}]O_2$. The oxidation state of Mn begins at $Mn^{3.63+}$ and increases to $Mn^{3.73+}$ during charging to 4.3 V. Upon discharging to 1.5 V, the oxidation state decreases to $Mn^{3.41+}$. Figure 6b presents the Fe K-edge spectra compared with Fe_2O_3 (Fe^{3+}) as a reference and the electrochemically $Fe^{3+/4+}$ redox pair during cycling. For the Ti K-edge spectra, the oxidation state of Ti remains Ti^{4+} during cycling, as observed in Figure 6c, as the spectra overlapped with the TiO_2 (Ti^{4+}) reference. We also employed X-ray photoelectron spectroscopy (XPS) to confirm the variation of binding energies for Mn, Fe, and Ti for $Na_{0.67}[(Mn_{0.78}Fe_{0.22})_{0.9}Ti_{0.1}]O_2$. The oxidation and reduction reactions were also evidenced in XPS data which presented reversible movements of Mn and Fe binding energies but remained constant for Ti (Figure S3, Supporting Information). These XANES and XPS results demonstrate that the substituted Ti does not participate in the electrochemical reaction but helps maintain the structure, resulting in a single-phase reaction upon electrochemical reaction in Na cells, which is likely responsible for the improvement of the electrode performance.

Because there is no direct information on the bonding energies of TiO_2 and MnO_2, the standard Gibbs free energy at 298 K was used as mentioned in Introduction. The Gibbs free energies of TiO_2 (Ti^{4+}) and MnO_2 (Mn^{4+}) are –888 and –465.2 kJ mol^{-1}, respectively, which indicates that the Ti–O bonds are stronger than the Mn–O bonds in the structure.[30] The stronger Ti–O bonds may suppress the movements of Mn–O and Fe–O by sharing the oxygen with Ti, presumably followed by the sequence of Mn–O–Ti–O–Fe in the transition metal layers. The average oxidation state of Mn after discharge was 3.41^+, which is higher than that of the discharged P′2-$Na_xMn^{3+}O_2$ ($x \approx 1$). In addition, Ceder et al.[31] recently explained the Jahn–Teller activity of $Fe^{4+}O_6$ octahedra, which results in buckling and distortion of Fe–O bonds, thereby facilitating Na^+ diffusion. The shared oxygen bonded with Ti is clearly beneficial in suppressing the movements of the (Mn, Fe)O_6 octahedra; therefore, the movement of the *c*-axis was only approximately 1.45%, as demonstrated by the *operando* SXRD data.

The extensively cycled P′2-$Na_{0.67}[(Mn_{0.78}Fe_{0.22})_{0.9}Ti_{0.1}]O_2$ electrodes were investigated using XRD (**Figure 7**a,b). Generally, structural degradation of postcycled electrodes is observed because of the large volume change and phase transition occurring during repetitive insertion and extraction of

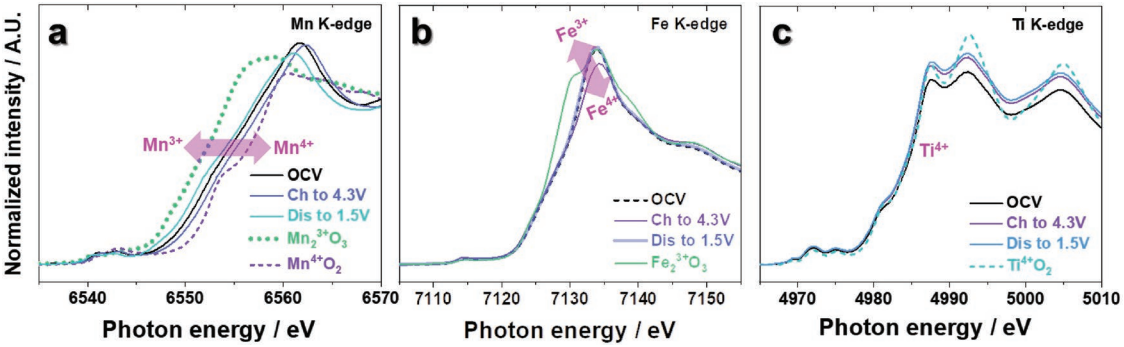

Figure 6. XANES spectra of a) Mn K-edge, b) Fe K-edge, c) Ti K-edge of P′2-$Na_{0.67}[(Mn_{0.78}Fe_{0.22})_{0.9}Ti_{0.1}]O_2$ electrodes: OCV, fully charged to 4.3 V, and fully discharged to 1.5 V.

alkali ions.[12,17,20,27,28] However, unlike for conventional electrodes, negligible change was induced in the crystal structure of the present $Na_{0.67}[(Mn_{0.78}Fe_{0.22})_{0.9}Ti_{0.1}]O_2$ after 100 cycles in Na cells; namely, the *a*-, *b*-, and *c*- lattice parameters increased from 2.8897 to 2.8900 Å, 5.2198 to 5.2206 Å, and 11.1892 to 11.8889 Å, respectively. Although the lattice parameters slightly deviated from those for the initial state after 200 cycles (2.8897 to 2.8907 Å for the *a*-axis, 5.2198 to 5.2297 Å for the *b*-axis, and 11.1892 to 11.1709 Å for the *c*-axis), the original crystal structure was maintained with high integrity. Normally, in active materials containing Mn^{3+}, disproportionation of Mn^{3+} toward Mn^{2+} and Mn^{4+} into the Na electrolyte occurs during cycling. In particular, the HF generated from decomposition of Na salts in the electrolyte at high voltage attacks the active materials, leading to dissolution of Mn^{2+}. The high proportion of Mn^{4+} in $Na_{0.67}$ $[(Mn_{0.78}Fe_{0.22})_{0.9}Ti_{0.1}]O_2$ electrodes, as observed in Figure 1e, may be one of the reasons for the structural stability without structural collapse. To further confirm this structural stability, the postcycled electrodes were also examined using TEM, and the results indicate that no surface degradation or exfoliation occurred after 200 cycles (Figure 7c). In addition, the SAED pattern of the postcycled electrode did not vary from that of the fresh material (Figure 7d). This result emphasizes the effect of Ti in substantially stabilizing the crystal structure with prolonged cycling observed on the surface and in the bulk (Figure 7e) and indicates that the morphology of the active material was not seriously damaged. The particle morphology of the fresh and post cycled $Na_{0.67}[(Mn_{0.78}Fe_{0.22})_{0.9}Ti_{0.1}]O_2$ were compared (Figure S4, Supporting Information). In general, HF is generated by degradation of electrolytic salt during high voltage operation and for long term cycling.[12,17,27] Notwithstanding, the $Na_{0.67}[(Mn_{0.78}Fe_{0.22})_{0.9}Ti_{0.1}]O_2$ active material did not show cracking or rupture even after 500 cycles at 5 C-rate. It is thought that the single phase reaction retaining the P′2 phase with minimized *c*-axis variation during de/sodiation is

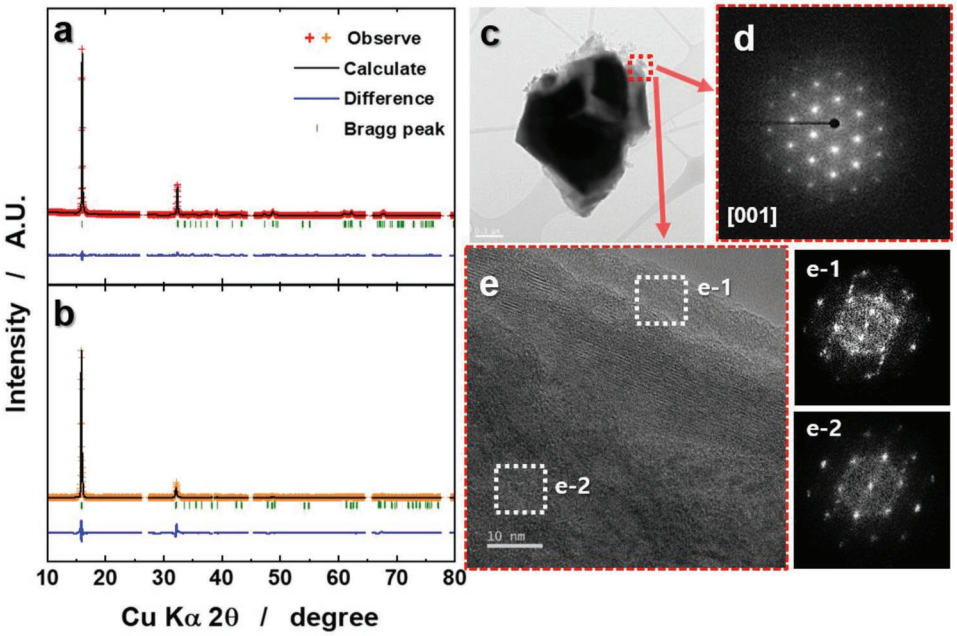

Figure 7. Rietveld refinement patterns of $Na_{0.67}[(Mn_{0.78}Fe_{0.22})_{0.9}Ti_{0.1}]O_2$ electrodes after a) 100 cycles and b) 200 cycles. c) Bright-field TEM image and d) resulting SAED patterns for $Na_{0.67}[(Mn_{0.78}Fe_{0.22})_{0.9}Ti_{0.1}]O_2$ electrode after 200 cycles. e) High-resolution TEM image and fast Fourier transform patterns of magnified parts: (e-1) outer surface and (e-2) bulk side of interior of $Na_{0.67}[(Mn_{0.78}Fe_{0.22})_{0.9}Ti_{0.1}]O_2$ electrode after 200 cycles.

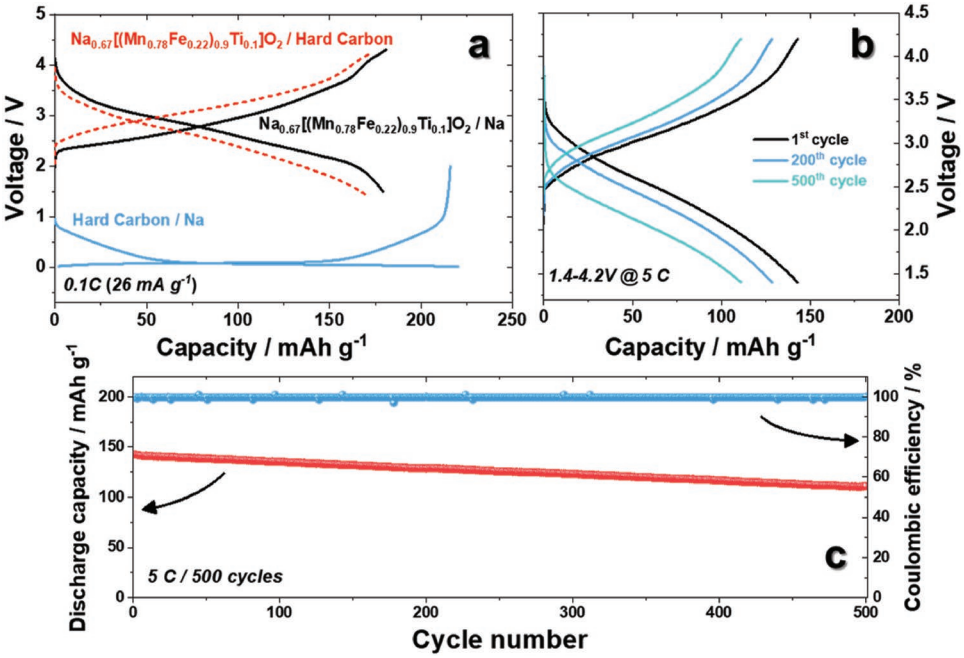

Figure 8. a) First charge and discharge curves of $Na_{0.67}[(Mn_{0.78}Fe_{0.22})_{0.9}Ti_{0.1}]O_2$ // Na metal half cell (black), $Na_{0.67}[(Mn_{0.78}Fe_{0.22})_{0.9}Ti_{0.1}]O_2$ // hard carbon full cell (red), and hard carbon // Na metal half cell (blue) and cycling performance of $Na_{0.67}[(Mn_{0.78}Fe_{0.22})_{0.9}Ti_{0.1}]O_2$ // hard carbon full cell at 0.1C. b) Charge–discharge curve measured at 5C and c) resulting cycling performances between 1.4 and 4.2 V.

the most plausible reason for the maintenance of the particle morphology for long term cycling test.

A full cell configured using $Na_{0.67}[(Mn_{0.78}Fe_{0.22})_{0.9}Ti_{0.1}]O_2$ and hard carbon was fabricated after adjusting the N/P capacity ratio to 1.2 to minimize the irreversibility at the 1st cycle (formation and grading after two cycles)[32] and the formation of a solid electrolyte interphase layer on the surface of the hard carbon anode (**Figure 8**a). The results revealed the excellent cyclability and good retention (≈80%) after 500 cycles (111 mAh g^{-1}) at 5C (1.3 A g^{-1}) (Figure 8b,c). Our findings indicate that P′2-$Na_{0.67}[(Mn_{0.78}Fe_{0.22})_{0.9}Ti_{0.1}]O_2$ materials are promising for the development of energy storage systems with long cycle life at high rates.

3. Conclusion

In summary, we introduce P′2-$Na_{0.67}[(Mn_{0.78}Fe_{0.22})_{0.9}Ti_{0.1}]O_2$ as a cathode material for SIBs to overcome the disadvantages of Mn-based layered structures, such as the Jahn–Teller effect of Mn^{3+} ions, which lead to structural degradation and poor cell performance. The partial substitution of Mn with Fe and Ti in $Na_{0.67}[(Mn_{0.78}Fe_{0.22})_{0.9}Ti_{0.1}]O_2$ brings about S-shaped charge and discharge curves, indicating the occurrence of a single phase reaction during de/sodiation. By suppressing the P′2 to OP4 phase transition, $Na_{0.67}[(Mn_{0.78}Fe_{0.22})_{0.9}Ti_{0.1}]O_2$ is able to deliver a high discharge capacity (≈180 mAh g^{-1}) for 200 cycles. Furthermore, a capacity retention of ≈80% is achieved for $Na_{0.67}[(Mn_{0.78}Fe_{0.22})_{0.9}Ti_{0.1}]O_2$ // hard carbon full cells for 500 cycles (111 mAh g^{-1}) at 5C (1.3 A g^{-1}). First-principles calculations reveal that $Na_{0.67}[(Mn_{0.78}Fe_{0.22})_{0.9}Ti_{0.1}]O_2$ requires a low activation barrier energy of ≈541 meV for Na^+ diffusion along the $Na1_1$–$Na1_2$ pathway in the *ab* plane. Our findings demonstrate the potential of P′2-$Na_{20.67}[(Mn_{0.78}Fe_{0.22})_{0.9}Ti_{0.1}]O_2$ as a promising cathode material for SIBs.

4. Experimental Section

Synthesis: P′2-$Na_{0.67}[(Mn_{0.78}Fe_{0.22})_{0.9}Ti_{0.1}]O_2$ powder was synthesized via ultrasonic spray pyrolysis.[20] The nitrate sources, $NaNO_3$ (Samchun), $Mn(NO_3)_2 \cdot 6H_2O$ (Sigma Aldrich), and $Fe(NO_3)_3 \cdot 9H_2O$ (Sigma Aldrich), with citric acid (Junsei) and sucrose (Samchun) as chelating agents were dissolved in distilled water, and then, the mixed solution was sprayed into a quartz tube heated at 500 °C to obtain the powders. Finally, the obtained powders were mixed with anatase TiO_2 (SAMCHUN) for 30 min in an agate mortar and then calcined at 1300 °C for 10 h in an air atmosphere.

Material Characterization: The crystal structures of the synthesized samples were characterized using XRD (Panalytical X'pert diffractometer, Empyrean) in the scanning range of 10°–100° (2θ) with a step size of 0.03°, and the resulting XRD patterns were refined using FullProf.[33] The particle morphology was examined using SEM (JXA-8100, JEOL) and high-resolution TEM (HR-TEM; JEM-3010, JEOL). In addition, elemental mappings of the synthesized samples were obtained using EDS (7200-H, Horiba). *Operando* synchrotron XRD and XANES spectroscopy were used to monitor the change in the crystal structure of the cathode materials in Na cells at the 9C and 8C beamlines of Pohang Accelerator Laboratory (PAL), Pohang, South Korea, respectively. The XPS measurements (PHI 5600, PerkinElmer) were performed in the macro mode (3 × 3 mm^2) using a Mg X-ray source to avoid the Auger lines produced when using an Al X-ray source. The samples were first transferred to a hermitically sealed transfer chamber (ULVAC) in a glovebox and then transferred to the vacuum chamber of the XPS machine to prevent exposure to air or water molecules during the XPS measurements.

Electrochemical Tests: The electrochemical properties were evaluated using R2032-type coin cells. Electrodes were fabricated by blending the active materials (85 wt%), conducting agents (7.5 wt%, KS-6 and Super-P with a weight ratio of 1:1), and polyvinylidene fluoride (PVDF;

7.5 wt%) with an appropriate amount of *N*-methyl-2-pyrrolidone (NMP) solution. The obtained slurry was applied on aluminum foil for cathode and dried at 110 °C in a vacuum oven. Discs were punched out of the dried electrodes (diameter: 14 φ, mass loading; ≈ 4.0 mg cm^{-2}) to assemble Na coin cells with a Na metal anode for the half cell in 0.5 M $NaPF_6$ in propylene carbonate (PC):fluorinated ethylene carbonate (FEC) (98:2 by volume) solution. The $NaPF_6$ in PC:FEC solution with the concentration over 0.5 M Na salt led to translucent solution, indicating the solubility limit of the $NaPF_6$ salt is around 0.5 M in PC:FEC solution (Figure S5, Supporting Information); hence, the 0.5 M $NaPF_6$ in PC:FEC electrolyte was used in this work.[12,17,34] Sodium metal (Alfa Aesar Co.) was used as the negative electrode for the half cells, which was pressed for the sodium plate in a glove box and were punched out (diameter: 16 φ) to prepare the Na metal electrode. Commercial hard carbon (Kureha) was also used as the negative electrode for full cell tests to evaluate the long-term cyclability at high rate (5C, 1.3 A g^{-1}). The hard carbon structure is highly turbostratic and disordered model in 2*H*-graphite with microstructure (Figure S6, Supporting Information).[35] Prior to fabricating hard carbon anode, pretreatment of the hard carbon was done to eliminate adhered water at 1000 °C for 2 h in Ar atmosphere. After then, the hard carbon anode was fabricated by blending the active materials and PVDF (10 wt%) with an appropriate amount of NMP solution. The obtained slurry was applied on copper foil for anode and dried at 80 °C in a vacuum oven. Discs were punched out of the dried electrodes (diameter: 16 φ, mass loading; ≈2.7 mg cm^{-2}) to assemble coin cells with the Na metal anode for coin type half cells and full cells in 0.5 M $NaPF_6$ in propylene carbonate (PC):fluorinated ethylene carbonate (FEC) (98:2 by volume) solution. The fabricated anodes were presodiated through direct contact with sodium metal (Alfa Aesar) in 0.5 M $NaPF_6$ electrolyte for 30 min to minimize the irreversibility during sodiation process. The cathode and hard carbon anode (a capacity ratio of negative and positive electrodes to be 1.2) were separated by a glass fiber separator (GB-100R, Whatman) in a R2032 coin cell. The used electrolyte in the coin full cell was ≈150 µL. Finally, the fabricated half cells and full cells were cycled in in the range of 1.5–4.3 and 1.4–4.2 V, respectively. The GITT measurement was conducted at a rate of 0.1C (26 mA g^{-1}) with 10 min rest and open-circuit periods of 1 h in 1.5–4.3 V.

First-Principles Calculations: Density functional theory (DFT) calculations were performed using the Vienna Ab initio Simulation Package (VASP).[36] Projector-augmented wave (PAW) pseudopotentials were used with a plane-wave basis set, as implemented in VASP.[37] Perdew–Burke–Ernzerhof (PBE) parametrization of the generalized gradient approximation (GGA) was used for the exchange-correlation functional.[38] The GGA+U method[39] was adopted to address the localization of the d-orbital in the Mn, Ti, and Fe ions, with U_{eff} values of 3.9, 1.5, and 4.0, respectively, based on previously determined data.[40] All the calculations were performed with an energy cutoff of 500 eV until the remaining force in the system converged to less than 0.05 eV $Å^{-1}$ per unit cell. NEB calculations were performed to determine the activation barrier of the Na^+ ion diffusion in the structure[41] A unit cell created by four formulaic units of P′2-$Na_{0.67}[(Mn_{0.78}Fe_{0.22})_{0.9}Ti_{0.1}]O_2$ was used, with one vacancy generated to model the Na^+ ionic diffusion. Five intermediate states were considered between the first and final images of a single Na^+ diffusion event. During the NEB calculation, all the structures were allowed to relax within the fixed lattice parameters.

Post-Cycling Analysis: After extensive cycling, the coin cells were disassembled in a glove box, and the electrodes were rinsed by immersion in a salt-free dimethyl carbonate (DMC) solvent for a day, and then, the electrodes were transferred to a vacuum chamber equipped in the glove box at 80 °C for a day. After then, the post cycled electrodes were used for ex situ XRD, XANES, and TEM analyses.

Supporting Information

Supporting Information is available from the Wiley Online Library or from the author.

Acknowledgements

Y.J.P. and J.U.C. contributed equally to this work. This research was supported by the Basic Science Research Program through the National Research Foundation, funded by the Ministry of Science and ICT of Korea (Grant No. NRF-2015M3D1A1069713, NRF- 2017R1A2A2A05069634), and (Grant No. 2017M2A2A6A01070834, Radiation Technology R&D program).

Conflict of Interest

The authors declare no conflict of interest.

Keywords

cathodes, first-principles calculations, full-cells, sodium, Ti substitution

Received: March 5, 2019
Revised: April 4, 2019
Published online: May 8, 2019

[1] C. Vaalma, D. Buchholz, M. Weil, S. Passerini, *Nat. Rev. Mater.* **2018**, *3*, 18013.
[2] a) L. P. Wang, L. Yu, X. Wang, M. Srinivasan, Z. J. Xu, *J. Mater. Chem. A* **2015**, *3*, 9353; b) N. Yabuuchi, K. Kubota, M. Dahbi, S. Komaba, *Chem. Rev.* **2014**, *114*, 11636.
[3] a) D. Kim, S.-H. Kang, M. Slater, S. Rood, J. T. Vaughey, N. Karan, M. Balasubramanian, C. S. Johnson, *Adv. Energy Mater.* **2011**, *1*, 333; b) K. Kang, Y. S. Meng, J. Bréger, C. P. Grey, G. Ceder, *Science* **2006**, *311*, 977; c) M. D. Slater, D. Kim, E. Lee, C. S. Johnson, *Adv. Energy Mater.* **2013**, *23*, 947.
[4] H. Pan, Y.-S. Hu, L. Chen, *Energy Environ. Sci.* **2013**, *6*, 2338.
[5] C. Nithya, S. Gopukumar, *Wiley Interdiscip. Rev.: Energy Environ.* **2015**, *4*, 253.
[6] J.-Y. Hwang, S.-T. Myung, Y.-K. Sun, *Chem. Soc. Rev.* **2017**, *46*, 3529.
[7] R. Stoyanova, D. Carlier, M. Sendova-Vassileva, M. Yoncheva, E. Zhecheva, D. Nihtianova, C. Delmas, *J. Solid State Chem.* **2010**, *183*, 1372.
[8] N. Yabuuchi, M. Kajiyama, J. Iwatate, H. Nishikawa, S. Hitomi, R. Okuyama, R. Usui, Y. Yamada, S. Komaba, *Nat. Mater.* **2012**, *11*, 512.
[9] L. B.-L. Guenne, P. Deniard, P. Biensan, C. Siret, R. Brec, *J. Mater. Chem.* **2000**, *10*, 2201.
[10] R. Berthelot, D. Carlier, C. Delmas, *Nat. Mater.* **2011**, *10*, 74.
[11] a) M. Guignard, C. Didier, J. Darriet, P. Bordet, E. Elkaïm, C. Delmas, *Nat. Mater.* **2013**, *12*, 74; b) M. Guignard, D. Carlier, C. Didier, M. R. Suchomel, E. Elkaïm, P. Bordet, R. Decourt, J. Darriet, C. Delmas, *Chem. Mater.* **2014**, *26*, 1538.
[12] J. H. Jo, J. U. Choi, A. Konarov, H. Yashiro, S. Yuan, L. Shi, Y.-K. Sun, S.-T. Myung, *Adv. Funct. Mater.* **2018**, *28*, 1705968.
[13] M. Yoncheva, R. Stoyanova, E. Zhecheva, E. Kuzmanova, M. Sendova-Vassileva, D. Nihtianova, D. Carlier, M. Guignard, C. Delmas, *J. Mater. Chem.* **2012**, *22*, 23418.
[14] a) J.-Y. Hwang, J. Kim, T.-Y. Yu, Y.-K. Sun, *Adv. Energy Mater.* **2019**, 1803346; b) C. Luo, A. Langrock, X. Fan, Y. Liang, C. Wang, *J. Mater. Chem. A* **2017**, *5*, 18214.
[15] a) R. J. Clément, J. Billaud, A. Robert Armstrong, G. Singh, T. Rojo, P. G. Bruce, C. P. Grey, *Energy Environ. Sci.* **2016**, *9*, 3240; b) N. Yabuuchi, R. Hara, K. Kubota, J. Paulsen, S. Kumakura, S. Komaba, *J. Mater. Chem. A* **2014**, *2*, 16851.

[16] G. Singh, N. Tapia-Ruiz, J. M. Lopez del Amo, U. Maitra, J. W. Somerville, A. R. Armstrong, J. Martinez de Ilarduya, T. Rojo, P. G. Bruce, *Chem. Mater.* **2016**, *28*, 5087.
[17] J. U. Choi, C. S. Yoon, Q. Zhang, P. Kaghazchi, Y. H. Jung, K.-S. Lee, D.-C. Ahn, Y.-K. Sun, S.-T. Myung, *J. Mater. Chem. A* **2019**, *7*, 202.
[18] S. Kumakura, Y. Tahara, K. Kubota, K. Chihara, S. Komaba, *Angew. Chem., Int. Ed.* **2016**, *55*, 12760.
[19] S. Kumakura, Y. Tahara, S. Sato, K. Kubota, S. Komaba, *Chem. Mater.* **2017**, *29*, 8958.
[20] J. U. Choi, Y. J. Park, J. H. Jo, L.-Y. Kuo, P. Kaghazchi, S.-T. Myung, *ACS Appl. Mater. Interfaces* **2018**, *10*, 40978.
[21] J. A. Dean, *Lange's Handbook of Chemistry, fourth ed.* (Ed: J. A. Dean), McGraw-Hill Inc., New York **1992**, p. 1466.
[22] F. Bella, A. B. Muñoz-García, F. Colò, G. Meligrana, A. Lamberti, M. Destro, M. Pavone, C. Gerbaldi, *ACS Omega* **2018**, *3*, 8440.
[23] X.-F. Luo, C.-H. Yang, Y.-Y. Peng, N.-W. Pu, M.-D. Ger, C.-T. Hsieh, J.-K. Chang, *J. Mater. Chem. A* **2015**, *3*, 10320.
[24] N. Wang, Q. Liu, B. Sun, J. Gu, B. Yu, W. Zhang, D. Zhang, *Sci. Rep.* **2018**, *8*, 9934.
[25] a) J.-H. Kim, S.-T. Myung, C. S. Yoon, I.-H. Oh, Y.-K. Sun, *Chem. Mater.* **2004**, *151*, A1911; b) S.-T. Myung, S. Komaba, K. Hosoya, N. Hirosaki, Y. Miura, N. Kumagai, *Chem. Mater.* **2005**, *17*, 2427.
[26] a) K. Kubota, I. Ikeuchi, T. Nakayama, C. Takei, N. Yabuuchi, H. Shiiba, M. Nakayama, S. Komaba, *J. Phys. Chem. C* **2015**, *119*, 166; b) N. Yabuuchi, Y. Kawamoto, R. Hara, T. Ishigaki, A. Hoshikawa, M. Yonemura, T. Kamiyama, S. Komaba, *Inorg. Chem.* **2013**, *52*, 9131.
[27] A. Konarov, J. U. Choi, Z. Bakenov, S.-T. Myung, *J. Mater. Chem. A* **2018**, *6*, 8558.
[28] J.-Y. Hwang, S.-T. Myung, J. U. Choi, C. S. Yoon, H. Yashiro, Y.-K. Sun, *J. Mater. Chem. A* **2017**, *5*, 23671.
[29] a) P.-F. Wang, H. Xin, T.-T. Zuo, Q. Li, X. Yang, Y.-X. Yin, X. Gao, X. Yu, Y.-G. Guo, *Angew. Chem., Int. Ed.* **2018**, *57*, 8178; b) P.-F. P.-F. Wang, H.-R. Yao, X.-Y. Liu, J.-N. Zhang, L. Gu, X.-Q. Yu, Y.-X. Yin, Y.-G. Guo, *Adv. Mater.* **2017**, *29*, 1700210.
[30] *The Oxide Handbook* (Eds: O. Kubaschewski, G. V. Samsonov), 2nd Ed., IFI/Plenum, New York and London **1982**, p. 761.
[31] X. Li, Y. Wang, D. Wu, L. Liu, S.-H. Bo, G. Ceder, *Chem. Mater.* **2016**, *28*, 6575.
[32] C.-H. Jo, J. U. Choi, H. Yashiro, S.-T. Myung, *J. Mater. Chem. A* **2019**, *7*, 3903.
[33] J. Carvajal, Abstracts of the Satellite Meeting on Powder Diffraction of the XV Congress of the IUCr **1990**.
[34] a) C.-Y. Yu, J.-S. Park, H.-G. Jung, K.-Y. Chung, D. Aurbach, Y.-K. Sun, S.-T. Myung, *Energy Environ. Sci.* **2015**, *8*, 2019; b) M. K. Cho, J. H. Jo, J. U. Choi, J. Kim, H. Yashiro, S. Yuan, L. Shi, Y.-K. Sun, S.-T. Myung, *Nano Energy* **2017**, *41*, 687.
[35] X. Dou, I. Hasa, D. Saurel, C. Vaalma, L. Wu, D. Buchholz, D. Bresser, S. Komaba, S. Passerini, *Mater. Today* **2019**, *23*, 87.
[36] G. Kresse, J. Furthmüller, *Comput. Mater. Sci.* **1996**, *6*, 15.
[37] P. E. Blöchl, *Phys. Rev. B* **1994**, *50*, 17953.
[38] J. P. Perdew, K. Burke, M. Ernzerhof, *Phys. Rev. Lett.* **1996**, *77*, 3865.
[39] V. I. Anisimov, *First-Principles Calculations of the Electronic Structure and Spectra of Strongly Correlated Systems: LDA + U Method*, Springer Nature, Berlin **1995**.
[40] a) A. Jain, G. Hautier, S. P. Ong, C. J. Moore, C. C. Fischer, K. A. Persson, G. Ceder, *Phys. Rev. B* **2011**, *84*, 045115; b) Y. Wang, J. Liu, B. Lee, R. Qiao, Z. Yang, S. Xu, X. Yu, L. Gu, Y.-S. Hu, W. Yang, K. Kang, H. Li, X.-Q. Yang, L. Chen, X. Huang, *Nat. Commun.* **2015**, *6*, 6401.
[41] G. Henkelman, B. P. Uberuaga, H. Jónsson, *J. Chem. Phys.* **2000**, *113*, 9901.